



CO and CO₂ Productions Rates of Comets Observed by NEOWISE within Year 1 of the Reactivated Mission

Adeline Gicquel¹ , James M. Bauer¹ , Emily A. Kramer² , Amy K. Mainzer³ , and Joseph R. Masiero⁴

¹Department of Astronomy, University of Maryland, College Park, MD 20740, USA; agicquel@umd.edu

²Jet Propulsion Laboratory, California Institute of Technology, 4800 Oak Grove Drive, Pasadena, CA 91109, USA

³Lunar and Planetary Laboratory, University of Arizona, Tucson, AZ 85721, USA

⁴IPAC, California Institute of Technology, Pasadena, CA 91125, USA

Received 2022 June 14; revised 2022 November 15; accepted 2022 December 2; published 2023 January 9

Abstract

We report on the observed fluxes of the comets detected by NEOWISE during the first year of operations after the spacecraft's reactivation. The sample included 57 comets. Of the comets detected, 30 were short-period comets (27 Jupiter-family comets, 1 Centaur, 2 Halley-type comets), and 27 were long-period comets. From the measured fluxes in the two NEOWISE bands, proxies for the gas production and coma dust are derived. We find a relationship between heliocentric distance, perihelion distance, and the gas-to-dust proxy fractions.

Unified Astronomy Thesaurus concepts: [Comets \(280\)](#); [Short period comets \(1452\)](#); [Long period comets \(933\)](#); [Infrared astronomy \(786\)](#)

1. Introduction

It is widely understood that, during the formation of the solar system, both CO and CO₂ were exceptionally common molecules in the presolar cloud and are consequently well preserved in cometary ice (Boogert et al. 2015; Willacy et al. 2022). The cometary ices CO and CO₂ are more volatile than water ice, and they are likely the main drivers of the coma gas activity of comets found at relatively large heliocentric distances, $R_h > 3$ au. By studying the materials released by the comets as they approach the Sun and become active, we can gain valuable insights into the nature and composition of the early solar system. Due to significant telluric contamination, CO₂ is detectable only from space (Bockelée-Morvan et al. 2004), owing to its self-absorption in Earth's atmosphere. Under certain circumstances, CO can be measured with ground-based infrared and radio (millimeter/submillimeter) telescopes (Dello Russo et al. 2009), though space-based telescopes, unobscured by the atmosphere, have considerable advantages of sensitivity and resolution for a given aperture and wavelength.

The Wide-field Infrared Survey Explorer (WISE) mission was launched in 2009 to survey the entire sky in the mid-infrared at 3.4, 4.6, 12, and 22 μm . These bands are respectively referred to as W1, W2, W3, and W4 (Wright et al. 2010). By 2010 October, the primary and secondary cryogen tanks were depleted, making the W3 (12 μm) and W4 (22 μm) channels inoperable. The mission continued to collect data until 2011 February, when the spacecraft was placed into hibernation (Mainzer et al. 2011). The spacecraft was then reactivated in 2013 October, and the mission was renamed Near Earth Object (NEO)WISE (Mainzer et al. 2014). The spacecraft restarted its W1 and W2 survey of the sky on 2013 December 13. The spatial resolutions of W1 and W2 are 6''1 and 6''4, respectively, given the FWHM of the

mean point-spread function (Wright et al. 2010; Cutri et al. 2012).

One major goal of NEOWISE was to constrain the CO and CO₂⁵ production in comets using the 4.6 μm band (Bauer et al. 2015). By measuring the infrared excess in W2 and accounting for other sources, such as nucleus or dust signal, we can identify the presence of CO+CO₂ emission. The W2 channel allows observation of the strong cometary emission lines, the CO₂ ν_3 vibrational fundamental band (4.23 μm), and the CO rovibrational fundamental bands (4.67 μm). The infrared Spitzer Space Telescope also observed comets at 3.6 and 4.5 μm (Reach et al. 2013). However, due to the wavelength resolution, in NEOWISE and Spitzer data, CO+CO₂ emission lines are encapsulated in a single broad 4.6 μm band. Consequently, it is not possible to separate the relative contributions of the two species. To date, researchers have relied on the higher-resolution AKARI data (Ootsubo et al. 2012) to sense CO and CO₂ separately in comets, and CO₂ has been shown to be the dominant volatile (Bauer et al. 2015, 2021). The emission line of CO is generally more than a factor of 11.6 times weaker than the CO₂ line (Crovisier & Encrenaz 1983). For this reason, and in consideration of observed abundances in comets (see Ootsubo et al. 2012 and Fougere et al. 2016), whereby the CO production rate (Q_{CO}) is commonly $\sim 10\%$ or less than the CO₂ production rate (Q_{CO_2}), the excess flux in the infrared in W2 is converted to $Q_{\text{CO}_2}^{\text{proxy}}$ and serves as a proxy for the total production rates of CO+CO₂.

In this paper, we describe the comet sample observed by NEOWISE within year 1 of the reactivated mission (2013 December–2014 December; NEOWISE-R Team 2020) and reported to the MPC by the NEOWISE moving object pipeline software (Mainzer et al. 2011, 2014; Cutri et al. 2012). We provide analyses of the dust and gas production rates for 57 comets. This sample contains 30 short-period comets (SPCs; 1 Centaur; 2 Halley-type comets, HTC) and 27 long-period comets (LPCs).



Original content from this work may be used under the terms of the [Creative Commons Attribution 4.0 licence](#). Any further distribution of this work must maintain attribution to the author(s) and the title of the work, journal citation and DOI.

⁵ Hereafter CO+CO₂ in the context of the NEOWISE measurements.

Table 1
Orbital Properties of Comets Observed by NEOWISE during Year 1 of the Reactivated Phase of the Mission

Object	Visit	i (deg)	e	q (au)	Phase Angle (deg)	Class	N_{obs}	Image Midpoint (MJD)
16P (Brooks 2)	A	4.26	0.56	1.47	28.5	JFC	13	56,963.0468
106P (Schuster)	B	20.15	0.59	1.55	29.8	JFC	10	56,979.60973
108P (Ciffreo)	B	13.10	0.54	1.71	34.3	JFC	18	56,893.5983
110P (Hartley 3)	A	11.69	0.31	2.48	23.4	JFC	16	56,933.84848
113P (Spitaler)	B	5.78	0.42	2.21	24.8	JFC	10	57,003.50698
117P (Helin-Roman-Alu 1)	A	8.70	0.25	3.06	19.2	JFC	11	56,778.59273
117P (Helin-Roman-Alu 1)	B	8.70	0.25	3.06	17.9	JFC	15	56,955.910 27
124P (Mrkos)	A	31.53	0.50	1.65	34.9	JFC	21	56,827.70765
134P (Kowal-Vavrova)	A	4.35	0.59	2.57	20.9	JFC	9	56,675.14157
134P (Kowal-Vavrova)	B	4.35	0.59	2.57	22.7	JFC	16	56,865.80458
174P (Echeclus)	A	4.34	0.46	5.82	9.6	Centaur	13	56,787.40954
191P (McNaught)	A	8.76	0.42	2.04	25.1	JFC	13	56,937.99378
193P (LINEAR-NEAT)	A	10.69	0.39	2.17	27.1	JFC	18	56,955.91186
209P (LINEAR)	C	21.24	0.67	0.97	26.6	JFC	19	56,950.44983
246P (NEAT)	A	15.97	0.28	2.88	15.4	JFC	14	56,840.24894
269P (Jedicke)	B	6.61	0.44	4.08	14.1	JFC	14	56,960.21958
273P (Pons-Gambart)	A	136.40	0.98	0.81	11.8	HTC	8	56,643.3139
284P (McNaught)	A	11.86	0.38	2.29	25.4	JFC	13	56,815.63891
287P (Christensen)	A	16.30	0.27	3.05	18.9	JFC	13	56,945.39127
290P (Jager)	A	19.05	0.65	2.16	27.5	JFC	15	56,747.35763
292P (Li)	A	24.36	0.59	2.52	22.8	JFC	20	56,666.21033
293P (Spacewatch)	A	9.06	0.42	2.11	26.3	JFC	12	56,777.04665
296P (Garradd)	A	25.20	0.48	1.83	31.6	JFC	18	56,786.22352
307P (LINEAR)	C	4.42	0.67	1.89	31.2	JFC	28	56,989.44056
405P (Lemmon)	D	9.37	0.69	1.12	38.0	JFC	27	56,799.94556
413P (Larson)	A	15.98	0.42	2.14	24.9	JFC	16	56,676.72043
413P (Larson)	C	15.98	0.42	2.14	27.3	JFC	13	56,874.55153
P/2012 B1 (PANSTARRS)	A	7.63	0.41	3.83	14.2	JFC	10	56,716.04824
P/2014 L2 (NEOWISE)	A	5.18	0.65	2.23	26.6	JFC	16	56,816.23109
P/2014 X1 (Elenin)	A	25.97	0.7 1	1.82	26.6	JFC	17	56,902.74207
C/2006 S3 (LONEOS)	A	166.03	1.00	5.13	8.1	LPC	10	56,674.15406
C/2006 S3 (LONEOS)	B	166.03	1.00	5.13	7.5	LPC	6	56,827.77698
C/2010 S1 (LINEAR)	A	125.34	1.00	5.90	9.1	LPC	8	56,772.99272
C/2011 J2-B (LINEAR)	B	122.80	1.00	3.44	14.7	LPC	12	56,871.81543
C/2011 J2-C (LINEAR)	B	122.80	1.00	3.44	14.7	LPC	13	56,871.81543
C/2011 KP36 (Spacewatch)	A	18.98	0.87	4.88	8.9	JFC	7	56,936.71359
C/2012 K1 (PANSTARRS)	A	142.43	1.00	1.05	20.2	LPC	12	56,714.06451
C/2012 K1 (PANSTARRS)	B	142.43	1.00	1.05	32.6	LPC	4	56,797.84754
C/2012 K1 (PANSTARRS)	D	142.43	1.00	1.05	31.1	LPC	12	56,998.76674
C/2012 X1 (LINEAR)	A	44.37	0.99	1.60	30.6	LPC	22	56,797.93967
C/2012 X1 (LINEAR)	B	44.37	0.99	1.60	16.5	LPC	20	56,962.41533
C/2013 A1 (Siding Spring)	A	129.03	1.00	1.40	14.9	LPC	10	56,673.64942
C/2013 A1 (Siding Spring)	B	129.03	1.00	1.40	32.7	LPC	9	56,866.8334
C/2012 E2 (Iwamoto)	A	21.86	0.99	1.41	14.5	LPC	14	56,653.62779
C/2013 G3 (PANSTARRS)	C	64.68	1.00	3.85	14.8	LPC	21	56,866.14247
C/2013 G6 (PANSTARRS)	A	124.09	0.99	2.05	21.8	LPC	9	56,641.84627
C/2013 N4 (Borisov)	A	37.04	0.97	1.21	22.3	LPC	11	56,689.64091
C/2013 P2 (PANSTARRS)	A	125.53	1.00	2.83	20.4	LPC	11	56,734.93754
C/2013 PE67 (Catalina-Spacewatch)	A	116.72	0.97	1.85	27.0	LPC	16	56,731.97056
C/2013 R1 (Lovejoy)	B	64.04	1.00	0.81	16.3	LPC	15	56,888.36547
C/2013 UQ4 (Catalina)	A	145.25	0.98	1.08	20.0	LPC	6	56,657.4112
C/2013 US10 (Catalina)	A	148.85	1.00	0.82	9.21	LPC	20	56,828.01071
C/2013 US10 (Catalina)	B	148.85	1.00	0.82	11.5	LPC	12	56,979.7095
C/2013 V1 (Boattini)	A	65.31	1.00	1.66	29.9	LPC	8	56,687.3622
C/2013 V4 (Catalina)	B	67.84	1.00	5.19	9.68	LPC	14	56,899.78044
C/2013 V5 (Oukaimeden)	A	154.87	1.00	0.61	17.2	LPC	7	56,719.63656
C/2013 Y2 (PANSTARRS)	A	29.42	0.99	1.92	30.6	LPC	9	56,783.61984
C/2013 Y2 (PANSTARRS)	B	29.42	0.99	1.92	31.1	LPC	22	56,790.13521
C/2014 C3 (NEOWISE)	A	151.78	0.98	1.86	31.3	LPC	6	56,703.00611
C/2014 C3 (NEOWISE)	B	151.78	0.98	1.86	25.7	LPC	8	56,788.17051
C/2014 E2 (Jacques)	A	156.39	1.00	0.66	21.9	LPC	9	56,687.99112
C/2014 N2 (PANSTARRS)	B	133.01	1.00	2.18	27.1	LPC	5	56,908.55454

Table 1
(Continued)

Object	Visit	i (deg)	e	q (au)	Phase Angle (deg)	Class	N_{obs}	Image Midpoint (MJD)
C/2014 N3 (NEOWISE)	A	61.63	1.00	3.88	13.2	LPC	7	56,842.42475
C/2014 Q1 (PANSTARRS)	B	43.07	1.00	0.31	15.1	LPC	10	56,983.2586
C/2014 Q2 (Lovejoy)	A	80.30	1.00	1.29	35.5	LPC	20	56,977.06118
C/2014 Q3 (Borisov)	B	89.95	0.94	1.65	35.0	HTC	16	56,936.21271
C/2014 Q3 (Borisov)	C	89.95	0.94	1.65	36.7	HTC	17	56,989.194,28
C/2014 R4 (Gibbs)	B	42.41	1.00	1.82	32.0	LPC	18	56,983.231,93

Note. The orbital parameters were provided by the JPL’s HORIZONS ephemeris service (<https://ssd.jpl.nasa.gov/>). The orbital properties include the orbital inclination i , orbital eccentricity e , and perihelion distance q . The phase angle, the class of the comets: short-period comets (SPCs; 1 Centaur; 2 Halley-type comets, HTCs) and long-period comets (LPCs), the number of observations (N_{obs}), and the image stack midpoint (MJD) are also included.

2. Observations

Observations of solar system objects obtained with the NEOWISE spacecraft are not targeted but rather are obtained when the survey covers the same region of sky where the object resides. The spacecraft may detect the comet multiple times at different parts of the sky. As explained by Bauer et al. (2013, 2015) and Rosser et al. (2018), all comet observations with multiple sets of detections during year 1 of the reactivated mission are divided into visits. The separation time between two visits may be several days, weeks, or months. Visits are typically ~ 13 exposures (i.e., a single pair of 7.7 s images collected by the spacecraft in the two channels, W1 and W2) over a time span of ~ 36 hr, but these values may vary considerably for individual visits. The number of frames in a visit varied from four to 28 in both the W1 and W2 bands (Table 1). These images were coaligned with the comets’ motion and coadded as described below. Figures 1 and 2 show the coadded images in both the W1 and W2 bands for SPCs and LPCs, respectively.

We analyzed visits from 2013 December to 2014 December. The sample included 57 comets. Of the comets detected, 30 were SPCs (27 JFCs; 1 Centaur; 2 HTCs), and 27 were LPCs. The observations included 11 comets that were detected and yielded significant infrared excess during multiple visits (i.e., the CO+CO₂ spectral line emission is strong enough to manifest as excess flux in the W2 band relative to the signal level in the W1). For 117P, 134P, 413P, C/2006 S2, C/2012 X1, C/2013 A1, C/2013 US10, C/2013 Y2, C/2014 C3, and C/2014 Q3, there were two visits that yielded IR excess. For C/2012 K1, there were three visits that yielded IR excess. The orbital properties, class, number of observations, and image stack midpoint of comets observed by NEOWISE during year 1 of the reactivated phase of the mission can be found in Table 1.

3. Analysis

Single-exposure images were coaligned with the comet’s motion and combined into a single coadd image. The coadds from each observation were created using the Image Co-addition with Optional Resolution Enhancement routine developed for the NEOWISE mission (Masci & Fowler 2009). Images with quality scores of zero (qual_frame = 0) or with bright background objects near the comet’s ephemeris position were excluded from the coadds. The qual_frame contains an integer ranging from zero (lowest quality) to 10 (best quality) that is obtained from a single-exposure frame set from which this entry was extracted by the quality-assurance process. To

ensure that there were no bright background objects, the images were compared to the AllWISE Image Atlas and Source Catalog (Cutri et al. 2012). An 11'' aperture was used to extract the counts from the coadded W1 and W2 images. The 11'' aperture is more than three times the FWHM of the image profile. There were no aperture corrections. The background was sampled using annulus apertures centered on the comet with inner and outer radii of 35'' and 65''. In the case of an extended source, the background was sampled using annulus apertures with an offset from the center of the comet with inner and outer radii of 1'' and 10''. The methodology described and employed in Wright et al. (2010) and Bauer et al. (2015, 2017, 2021) was used to convert the counts to flux values (Table 2). The signal-to-noise ratio is dependent on the number of frames and how crowded the background field was. No color corrections were applied in the flux conversions from W1 and W2 in order to not overestimate the gas production rate. The reflected component of the observed flux follows a solar spectrum and has a color correction of ≈ 1 . For each object, a plot (as shown in Figure 3) was produced to represent the reflected light flux and thermal signal. Because the signal in W1 (3.4 μm) is dominated by the dust signal, it can be used to constrain the dust signal in W2. The reflected light emission flux is constrained by data in the W1 band. The thermal emission flux is approximated from data in the W1 band. The thermal signal was extrapolated using a blackbody temperature for dust with a visible wavelength albedo $p_V \approx 0.05$ and an emissivity $\epsilon = 0.9$ (Bauer et al. 2015, 2021). The data provided by the W1 band were used to calculate $Af\rho$, as explained in Rosser et al. (2018). The excess W2 flux (as shown in Figure 3) is assumed to be due to Q_{CO_2} for the purpose of creating a proxy for CO+CO₂ production because the emission line of CO is generally more than a factor of 11.6 times weaker than the CO₂ line (Crovisier & Encrenaz 1983). The conversion of the excess W2 signal to $Q_{\text{CO}_2}^{\text{proxy}}$ is explained in detail in Rosser et al. (2018). The derived dust and production rates are listed in Table 2.

As mentioned in Bauer et al. (2015, 2021), there is a critical difference between the measurements taken in the NEOWISE reactivation and postcryo mission phases and those from the WISE/NEOWISE cryogenic mission phases. During the fully cryogenic phase, the dust thermal component of the signal can be constrained by the W3 and W4 band signal, and the total dust contribution can be extrapolated. Thus, CO+CO₂ contributions can be measured for comets inward of ~ 2 au. However, in the NEOWISE reactivation mission and postcryo phases with W1 signal alone, the thermal signal at comet

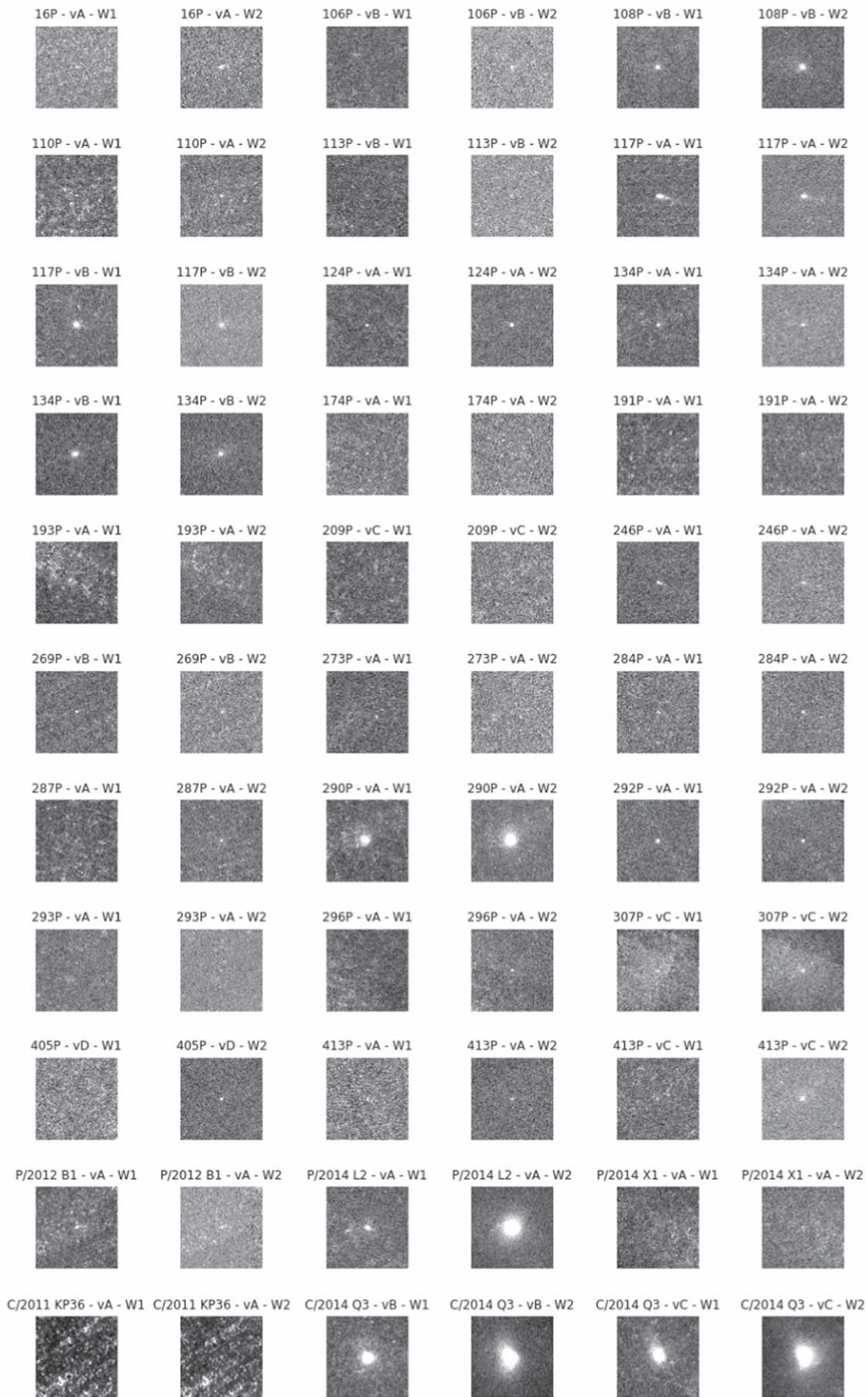


Figure 1. NEOWISE observations for SPCs in the W1 and W2 bands. The images are oriented with north up and east to the left. The images are $6' \times 6'$.

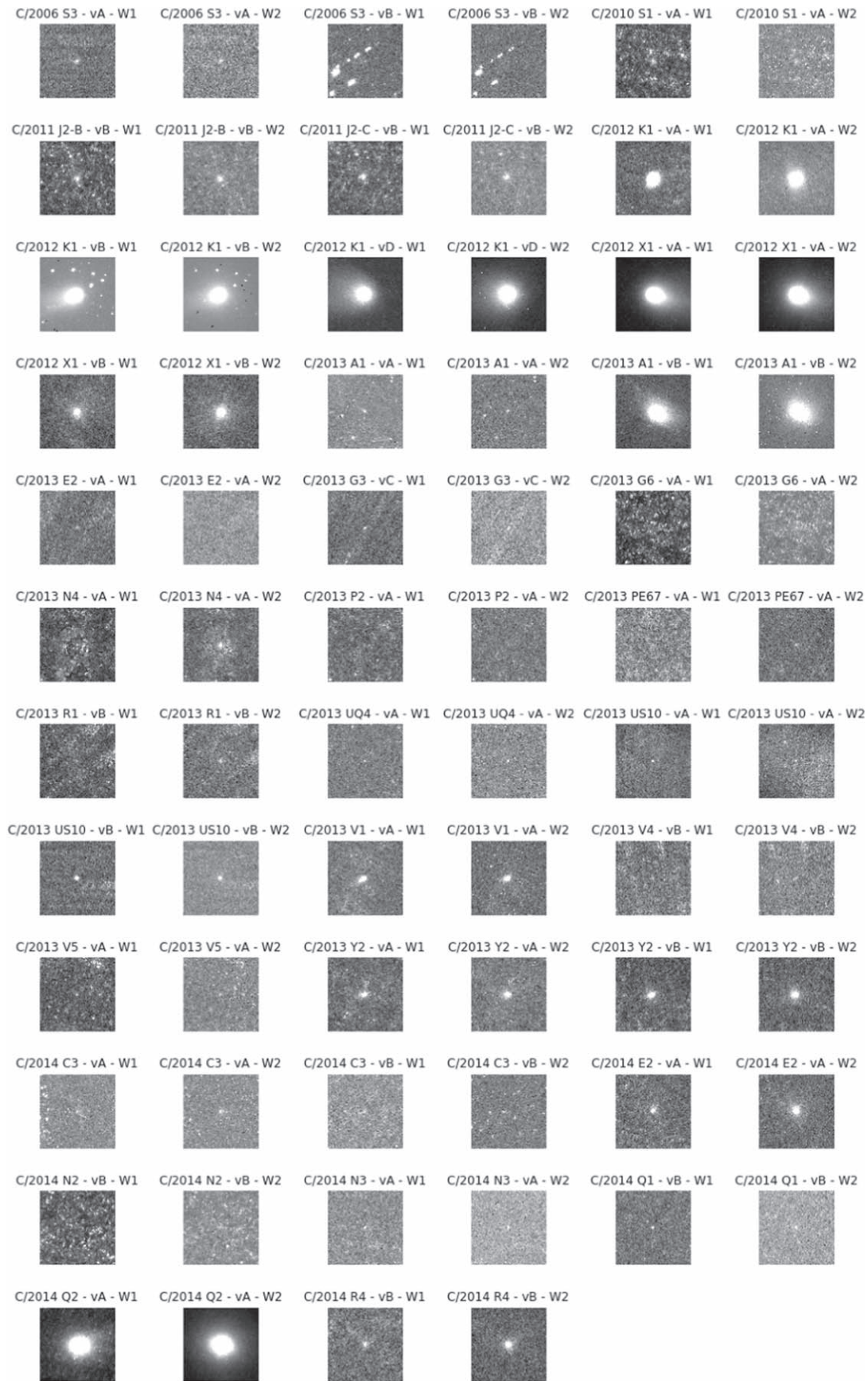


Figure 2. NEOWISE observations for LPCs in the W1 and W2 bands. The images are oriented with north up and east to the left. The images are $6' \times 6'$.

Table 2
Analysis of Comets Observed by NEOWISE during Year 1 of the Reactivated Phase of the Mission

Object	Visit	R_h (au)	Δ (au)	W1 Flux (mJy)	W2 Flux (mJy)	$Q_{\text{CO}_2}^{\text{proxy}}$ (molecules s ⁻¹)	$Af\rho$ (cm)	T_{eff} (K)
16P (Brooks 2)	A	2.08	1.79	0.11 ± 0.03	0.34 ± 0.08	(4.60 ± 0.56) × 10 ²⁵	15.32 ± 3.88	198.31
106P (Schuster) ^a	B	1.98	1.66	0.05 ± 0.02	0.34 ± 0.08	(4.61 ± 0.50) × 10 ²⁵	6.26 ± 1.83	203.25
108P (Ciffreo) ^a	B	1.79	1.42	0.61 ± 0.14	2.89 ± 0.64	(2.68 ± 0.10) × 10 ²⁶	49.52 ± 11.18	213.77
110P (Hartley 3)	A	2.52	2.27	0.13 ± 0.03	0.30 ± 0.07	(6.21 ± 0.86) × 10 ²⁵	32.63 ± 8.22	180.16
113P (Spitaler)	B	2.34	2.08	0.09 ± 0.02	0.25 ± 0.06	(4.27 ± 0.66) × 10 ²⁵	19.25 ± 5.01	186.96
117P (Helin-Roman-Alu 1)	A	3.06	2.83	0.84 ± 0.19	1.00 ± 0.22	(2.34 ± 0.25) × 10 ²⁶	401.08 ± 89.92	163.50
117P (Helin-Roman-Alu 1)	B	3.22	3.01	0.93 ± 0.21	0.93 ± 0.21	(2.03 ± 0.28) × 10 ²⁶	524.10 ± 117.27	159.38
124P (Mrkos) ^a	A	1.77	1.42	0.18 ± 0.04	1.49 ± 0.33	(1.50 ± 0.07) × 10 ²⁶	14.10 ± 3.38	214.97
134P (Kowal-Vavrova)	A	2.76	2.55	0.36 ± 0.08	0.61 ± 0.14	(1.41 ± 0.15) × 10 ²⁶	125.91 ± 28.96	172.15
134P (Kowal-Vavrova)	B	2.63	2.36	0.51 ± 0.12	0.78 ± 0.18	(1.45 ± 0.14) × 10 ²⁶	151.04 ± 34.26	176.36
174P (Echeclus)	A	6.05	5.92	0.08 ± 0.02	0.11 ± 0.03	(1.57 ± 0.55) × 10 ²⁶	315.79 ± 83.80	116.28
191P (McNaught)	A	2.35	2.10	0.11 ± 0.03	0.24 ± 0.06	(4.05 ± 0.65) × 10 ²⁵	21.93 ± 5.66	186.57
193P (LINEAR-NEAT)	A	2.18	1.88	0.10 ± 0.03	0.25 ± 0.06	(3.55 ± 0.55) × 10 ²⁵	16.43 ± 4.25	193.70
209P (LINEAR)	C	2.21	1.93	0.03 ± 0.01	0.11 ± 0.03	(1.85 ± 0.41) × 10 ²⁵	5.54 ± 1.83	192.38
246P (NEAT)	A	3.82	3.64	0.21 ± 0.05	0.24 ± 0.06	(9.64 ± 2.32) × 10 ²⁵	196.17 ± 46.54	146.33
269P (Jedicke)	B	4.08	3.91	0.17 ± 0.04	0.23 ± 0.06	(1.32 ± 0.27) × 10 ²⁶	198.99 ± 48.01	141.59
273P (Pons-Gambart)	A	4.81	4.66	0.03 ± 0.01	0.14 ± 0.04	(1.85 ± 0.34) × 10 ²⁶	55.80 ± 20.67	130.41
284P (McNaught)	A	2.36	2.09	0.12 ± 0.03	0.35 ± 0.08	(6.42 ± 0.77) × 10 ²⁵	25.72 ± 6.43	186.17
287P (Christensen)	A	3.08	2.87	0.15 ± 0.04	0.45 ± 0.11	(1.77 ± 0.18) × 10 ²⁶	74.69 ± 18.36	162.96
290P (Jager)	A	2.16	1.86	1.39 ± 0.31	4.94 ± 1.09	(7.56 ± 0.22) × 10 ²⁶	217.12 ± 48.31	194.60
292P (Li)	A	2.53	2.30	0.32 ± 0.07	0.45 ± 0.10	(7.14 ± 1.03) × 10 ²⁵	83.44 ± 19.29	179.81
293P (Spacewatch)	A	2.27	1.97	0.03 ± 0.01	0.11 ± 0.03	(1.84 ± 0.44) × 10 ²⁵	5.82 ± 2.03	189.83
296P (Garradd) ^a	A	1.92	1.60	0.08 ± 0.02	0.26 ± 0.06	(2.81 ± 0.41) × 10 ²⁵	8.56 ± 2.27	206.40
307P(LINEAR) ^a	C	1.90	1.60	0.09 ± 0.02	0.57 ± 0.13	(6.91 ± 0.58) × 10 ²⁵	9.26 ± 2.41	207.49
405P (Lemmon) ^a	D	1.63	1.23	0.04 ± 0.01	0.29 ± 0.07	(2.18 ± 0.26) × 10 ²⁵	2.18 ± 0.68	224.01
413P (Larson)	A	2.33	2.09	0.08 ± 0.02	0.29 ± 0.07	(5.46 ± 0.69) × 10 ²⁵	16.86 ± 4.43	187.37
413P (Larson)	C	2.21	1.89	0.14 ± 0.03	0.77 ± 0.17	(1.33 ± 0.09) × 10 ²⁶	22.76 ± 5.60	192.38
P/2012 B1 (PANSTARRS)	A	4.02	3.83	0.39 ± 0.09	0.38 ± 0.09	(1.36 ± 0.33) × 10 ²⁶	436.85 ± 100.24	142.64
P/2014 L2 (NEOWISE)	A	2.26	1.98	0.89 ± 0.20	9.80 ± 2.16	(2.98 ± 0.05) × 10 ²⁷	273.85 ± 61.33	175.36
P/2014 X1 (Elenin)	A	2.25	1.96	0.04 ± 0.01	0.16 ± 0.04	(2.71 ± 0.49) × 10 ²⁵	7.22 ± 2.28	190.67
C/2006 S3 (LONEOS)	A	6.98	6.88	0.42 ± 0.10	0.48 ± 0.12	(9.44 ± 1.52) × 10 ²⁶	2 518.55 ± 575.62	108.25
C/2006 S3 (LONEOS)	B	7.73	7.62	0.19 ± 0.05	0.31 ± 0.08	(1.04 ± 0.20) × 10 ²⁷	1 532.95 ± 372.55	102.87
C/2010 S1 (LINEAR)	A	6.37	6.23	0.65 ± 0.15	0.55 ± 0.13	(4.91 ± 1.29) × 10 ²⁶	2 963.15 ± 669.20	113.32
C/2011 J2-B (LINEAR)	B	3.99	3.82	0.79 ± 0.18	1.32 ± 0.30	(8.11 ± 0.58) × 10 ²⁶	862.47 ± 193.71	143.18
C/2011 J2-C (LINEAR)	B	3.99	3.82	0.66 ± 0.15	1.07 ± 0.24	(6.38 ± 0.52) × 10 ²⁶	722.81 ± 162.99	143.18
C/2011 KP36 (Spacewatch)	A	6.45	6.35	0.82 ± 0.19	1.82 ± 0.41	(4.29 ± 0.29) × 10 ²⁷	3 887.23 ± 926.67	112.61
C/2012 K1 (PANSTARRS)	A	2.86	2.63	6.79 ± 1.50	12.20 ± 2.69	(3.22 ± 0.07) × 10 ²⁷	2 628.35 ± 579.44	169.12
C/2012 K1 (PANSTARRS) ^a	B	1.87	1.54	31.41 ± 6.91	90.48 ± 19.90	(8.49 ± 0.06) × 10 ²⁷	3 033.16 ± 667.44	209.14
C/2012 K1 (PANSTARRS) ^a	D	1.91	1.61	16.38 ± 3.61	49.11 ± 10.81	(5.10 ± 0.05) × 10 ²⁷	1 726.51 ± 380.09	206.94
C/2012 X1 (LINEAR) ^a	A	1.98	1.65	35.41 ± 7.79	130.20 ± 28.64	(1.57 ± 0.01) × 10 ²⁸	4 112.45 ± 904.88	203.25
C/2012 X1 (LINEAR)	B	3.47	3.30	0.96 ± 0.21	3.69 ± 0.82	(2.09 ± 0.07) × 10 ²⁷	684.05 ± 153.01	153.53
C/2013 A1 (Siding Spring)	A	3.82	3.67	0.38 ± 0.09	0.50 ± 0.12	(2.32 ± 0.34) × 10 ²⁶	370.72 ± 85.05	146.33
C/2013 A1 (Siding Spring) ^a	B	1.88	1.54	7.00 ± 1.54	20.67 ± 4.55	(1.98 ± 0.03) × 10 ²⁷	683.73 ± 150.72	208.59
C/2013 E2 (Iwamoto)	A	3.91	3.74	0.14 ± 0.03	0.18 ± 0.05	(8.95 ± 2.29) × 10 ²⁵	114.06 ± 35.45	144.64
C/2013 G3 (PANSTARRS)	C	3.97	3.80	0.11 ± 0.03	0.18 ± 0.04	(1.06 ± 0.22) × 10 ²⁶	113.04 ± 28.79	143.54
C/2013 G6 (PANSTARRS)	A	2.65	2.44	0.38 ± 0.09	0.91 ± 0.21	(2.20 ± 0.18) × 10 ²⁶	117.24 ± 25.71	175.69
C/2013 N4 (Borisov)	A	2.59	2.35	0.25 ± 0.06	1.16 ± 0.26	(3.01 ± 0.17) × 10 ²⁶	71.81 ± 17.05	177.71
C/2013 P2 (PANSTARRS)	A	2.85	2.65	0.04 ± 0.01	0.12 ± 0.03	(3.97 ± 0.84) × 10 ²⁵	14.78 ± 4.73	169.41
C/2013 PE67 (Catalina-Spacewatch)	A	2.19	1.95	0.08 ± 0.02	0.30 ± 0.07	(5.03 ± 0.60) × 10 ²⁵	12.82 ± 3.41	193.26
C/2013 R1 (Lovejoy)	B	3.60	3.41	0.15 ± 0.04	0.47 ± 0.11	(2.81 ± 0.28) × 10 ²⁶	116.92 ± 28.76	150.74
C/2013 UQ4 (Catalina)	A	2.87	2.65	0.13 ± 0.03	0.75 ± 0.17	(1.82 ± 0.13) × 10 ²⁶	35.74 ± 8.85	168.82
C/2013 US10 (Catalina)	A	6.35	6.20	0.21 ± 0.05	0.33 ± 0.08	(6.09 ± 1.06) × 10 ²⁶	955.16 ± 226.37	113.50
C/2013 US10 (Catalina)	B	4.90	4.75	0.73 ± 0.16	1.01 ± 0.23	(8.70 ± 0.81) × 10 ²⁶	1 504.50 ± 338.22	129.20
C/2013 V1 (Boattini) ^a	A	1.97	1.65	1.83 ± 0.41	3.43 ± 0.76	(3.09 ± 0.15) × 10 ²⁶	210.24 ± 46.65	203.77
C/2013 V4 (Catalina)	B	5.99	5.86	0.09 ± 0.02	0.22 ± 0.05	(4.18 ± 0.69) × 10 ²⁶	352.87 ± 91.60	116.86
C/2013 V5 (Oukaimeden)	A	3.35	3.14	0.26 ± 0.06	0.37 ± 0.09	(1.32 ± 0.21) × 10 ²⁶	163.43 ± 38.32	156.26
C/2013 Y2 (PANSTARRS) ^a	A	1.97	1.64	1.13 ± 0.25	3.33 ± 0.74	(3.71 ± 0.14) × 10 ²⁶	128.78 ± 28.74	203.77
C/2013 Y2 (PANSTARRS) ^a	B	1.96	1.65	1.06 ± 0.24	3.17 ± 0.70	(3.55 ± 0.14) × 10 ²⁶	120/17 ± 26.83	204.29
C/2014 C3 (NEOWISE) ^a	A	1.90	1.59	0.30 ± 0.07	0.95 ± 0.22	(9.92 ± 0.73) × 10 ²⁵	30.41 ± 7.08	207.49
C/2014 C3 (NEOWISE)	B	2.32	2.00	0.10 ± 0.03	0.13 ± 0.04	(1.40 ± 0.51) × 10 ²⁵	20.17 ± 5.17	187.77
C/2014 E2 (Jacques)	A	2.63	2.39	0.75 ± 0.17	2.71 ± 0.60	(7.07 ± 0.27) × 10 ²⁶	222.79 ± 50.07	176.36
C/2014 N2 (PANSTARRS)	B	2.21	1.95	0.40 ± 0.09	0.82 ± 0.19	(1.12 ± 0.11) × 10 ²⁶	69.05 ± 16.18	196.38

Table 2
(Continued)

Object	Visit	R_h (au)	Δ (au)	W1 Flux (mJy)	W2 Flux (mJy)	$Q_{\text{CO}_2}^{\text{proxy}}$ (molecules s $^{-1}$)	$Af\rho$ (cm)	T_{eff} (K)
C/2014 N3 (NEOWISE)	A	4.45	4.29	0.24 ± 0.06	0.35 ± 0.08	$(2.57 \pm 0.41) \times 10^{26}$	363.40 ± 85.49	135.58
C/2014 Q1 (PANSTARRS)	B	3.79	3.61	0.24 ± 0.06	0.41 ± 0.10	$(2.21 \pm 0.29) \times 10^{26}$	226.40 ± 53.19	146.91
C/2014 Q2 (Lovejoy) ^a	A	1.70	1.35	45.04 ± 9.91	151.42 ± 33.31	$(1.06 \pm 0.01) \times 10^{28}$	$3\,140.56 \pm 690.96$	219.35
C/2014 Q3 (Borisov) ^a	B	1.74	1.39	2.78 ± 0.62	11.14 ± 2.46	$(9.07 \pm 0.18) \times 10^{26}$	209.65 ± 46.38	216.82
C/2014 Q3 (Borisov) ^a	C	1.65	1.32	3.31 ± 0.73	14.17 ± 3.12	$(9.87 \pm 0.18) \times 10^{26}$	212.25 ± 46.91	222.65
C/2014 R4 (Gibbs) ^a	B	1.86	1.52	0.22 ± 0.05	1.72 ± 0.38	$(1.97 \pm 0.09) \times 10^{26}$	20.97 ± 4.94	209.71

Notes. The parameters include the heliocentric distance R_h , Earth–comet distance Δ , W1 and W2 flux measurements, gas production rate $Q_{\text{CO}_2}^{\text{proxy}}$, dust production rate $Af\rho$, and effective dust temperature T_{eff} .

^a The results should be used with caution due to the possible contribution of the nucleus ($R_h < 2$ au). However, for comets C/2012 K1, C/2012 X1, C/2013 A1, C/2014 Q2, and C/2014 Q3, the signal should be dominated by the coma and not the nucleus (extended coma).

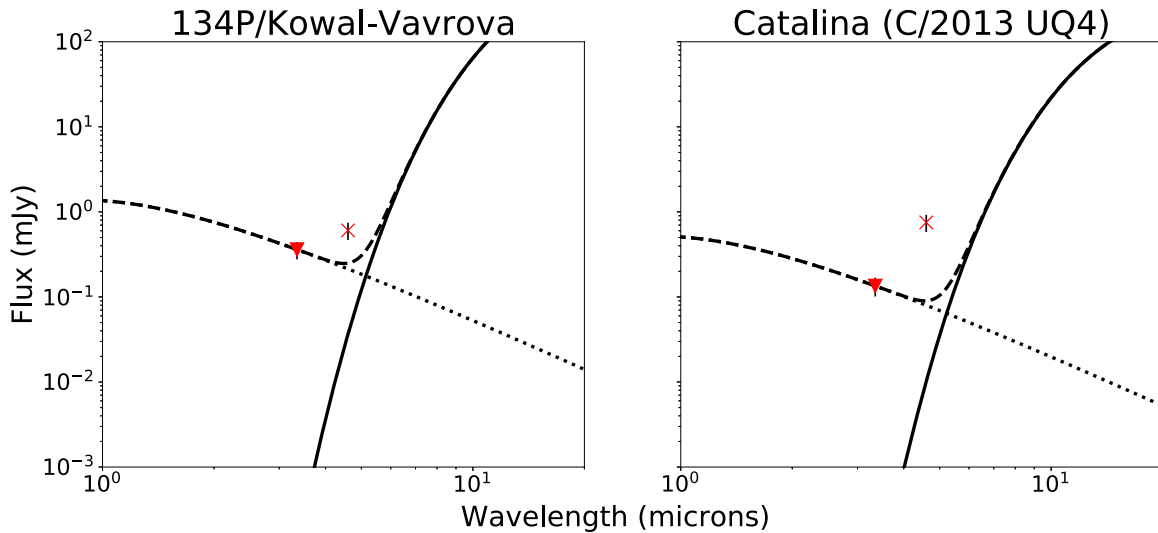


Figure 3. NEOWISE observations of the SPC 134P/Kowal–Vavrova at 2.76 au (visit A) and the LPC C/2013 UQ4 (Catalina) at 2.87 au (visit A). The flux from 3.4 (red triangle) and 4.6 (red cross) μm is shown. Also, the reflected light model (dotted line), thermal model (solid line), and combined signal (dashed line) are overplotted.

heliocentric distances of $\ll 2$ au begins to dominate over the gas emission (Reach et al. 2013; Bauer et al. 2015). Hence, there are a number of competing factors that may introduce biases in the sample, especially in relation to CO+CO₂ production. While the comets are closer to the Sun, they also may be more easily detected, since they are brighter. However, as the comet comes nearer to the Sun than 2 au, the CO+CO₂ emission must be significantly greater to be identified over the rising and competing dust thermal signal. Where CO and CO₂ production rates increase as $\sim R_h^{-2}$ (see Section 4), Figure 3 shows how the thermal edge of the dust signal moves to shorter wavelengths with diminishing R_h , such that the dust signal can dominate over the CO+CO₂ signal. In the instance of 134P shown in Figure 3, the thermal dust signal peaks at several hundred times the CO+CO₂ gas signature. Only a few comet observations here with identified CO+CO₂ emission excess were detected when the comets were within 2 au of the Sun. However, the results for comets with $R_h < 2$ au should be used with caution due to the fact that the nucleus contribution might not always be negligible.

The bright comet C/2014 Q3 (Borisov) shows an extended coma in the W1 and W2 bands (Figure 4) that can indicate the nature of the coma emission, i.e., whether it has significant gas or dust components at the observed wavelengths. Dust is more

subject to radiation pressure effects, and the W1 band should be dominated by dust continuum. The dust-subtracted image of the W2 signal, shown in Figure 4(c), revealed a gas-dominated coma. Both the W1 and W2 bands were background-subtracted, and the W1 image was rescaled to the computed dust signal at 4.6 μm (Figure 3) and subtracted from the W2 image. We added the contours that were obtained from Figure 4(a) to Figure 4(c). The remaining signal, presumably dominated by CO or CO₂ gas emission, does not match the direction of the anti-Sun dust tail in the W1 image (Figure 4(a)).

Observations with NEOWISE of five comets in our sample were previously reported by Bauer et al. (2015) and Rosser et al. (2018). Observations of comets P/2014 L2, C/2006 S3, C/2014 C3, and C/2014 N3 were reported by Bauer et al. (2015). Observations of comet C/2014 Q3 were reported by Rosser et al. (2018). Reported observations of comets P/2014 L2, C/2014 C3, C/2014 N3, and C/2014 Q3 were made at the same time as these observations, and the results were in agreement. Reported observations of comet C/2006 S3 were not made at the same time as these observations but rather were taken during the WISE prime mission during its cryogenic phase.

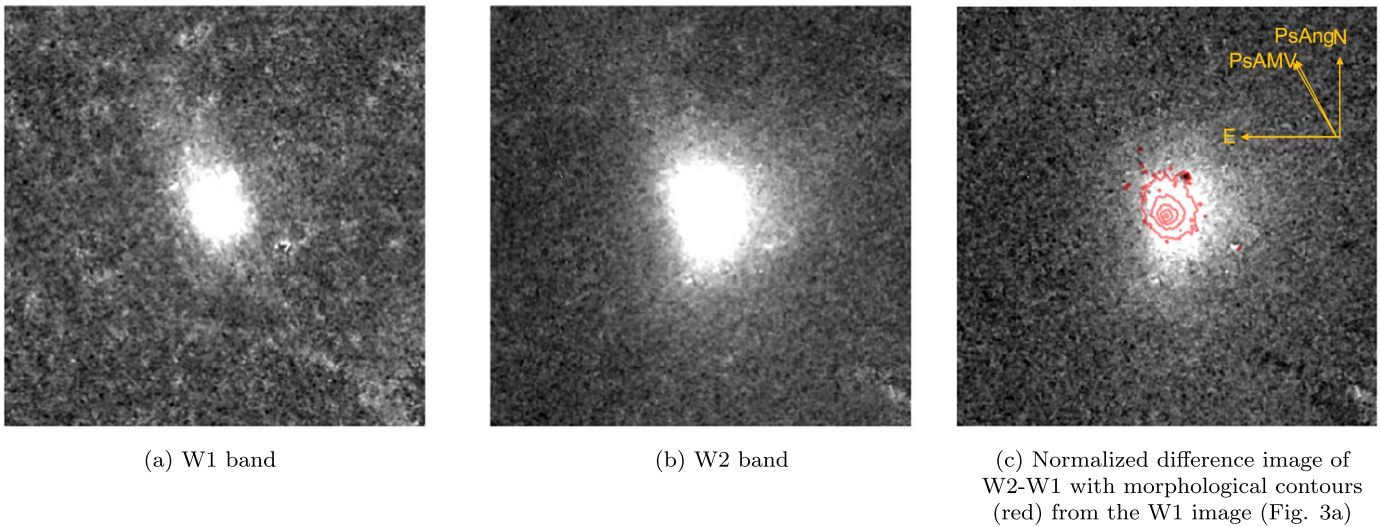


Figure 4. NEOWISE observations of comet C/2014 Q3 (Borisov) visit C. The images are oriented with north up and east to the left. The images are $6' \times 6'$. The PsAng and PsAMV were obtained using JPL's Horizons. Here PsAng is an indicator of the comet's gas tail orientation in the sky (antisunward direction), and PsAMV is an indicator of the comet's dust tail orientation.

4. Discussion

We examined the correlation between the heliocentric distance R_h , perihelion distance q , and distance from perihelion $R_h - q$ as a function of the independent variables in our study ($Af\rho$, $Q_{\text{CO}_2}^{\text{proxy}}$, $Q_{\text{CO}_2}^{\text{proxy}}/Af\rho$). The results of the heliocentric distance R_h as a function of $Af\rho$, $Q_{\text{CO}_2}^{\text{proxy}}$, and $Q_{\text{CO}_2}^{\text{proxy}}/Af\rho$ are shown in Figures 5(a) and (b) and 6(a). The results of $Q_{\text{CO}_2}^{\text{proxy}}/Af\rho$ as a function of the perihelion distance q are shown in Figure 6(b). The results of $Q_{\text{CO}_2}^{\text{proxy}}/Af\rho$ as a function of the distance from perihelion $R_h - q$ are shown in Figure 6(c). We divided the comets into two groups: SPCs and LPCs. We included the Centaur in the SPC group. The HTC comet C/2014 Q3 (Borisov) was previously included in the LPC group but is now included in the SPC group. We noted that the comet C/2011 KP36 (Spacewatch) was previously categorized as an LPC but is now categorized as a JFC and included in the SPC group. We used the same method as Bauer et al. (2015) and Rosser et al. (2018) by calculating both the Spearman rank coefficient (ρ_s) and Kendall τ (τ). However, the calculation of τ might be more reliable for a smaller sample size. The main difference between τ and ρ_s is that the calculations of τ are based on concordant and discordant pairs, and the calculations of ρ_s are based on deviations. The value of ρ_s or τ can range from -1 to 1 . Values near 1 indicate a correlation. Values near -1 indicate an anticorrelation. Values near 0 indicate no correlation.

The relationship between the heliocentric distance R_h and the dust production rate is shown in Figure 5(a). The results of the Kendall τ test were $\tau = 0.46$ and 0.22 for SPCs and LPCs, respectively. The results of the Spearman test were $\rho_s = 0.57$ and 0.24 for SPCs and LPCs, respectively. The results indicated that there is little to no correlation between $Af\rho$ and R_h .

The relationship between the heliocentric distance R_h and the gas production rate is shown in Figure 5(b). The results of the Kendall τ test were $\tau = 0.19$ and -0.01 for SPCs and LPCs, respectively. The results of the Spearman test were $\rho_s = 0.22$ and -0.11 for SPCs and LPCs, respectively. The results indicated that there is little to no correlation between $Q_{\text{CO}_2}^{\text{proxy}}$ and R_h .

The relationship between the heliocentric distance R_h and the gas-to-dust rate $Q_{\text{CO}_2}^{\text{proxy}}/Af\rho$ is shown in Figure 6(a). The results of the Kendall τ test were $\tau = -0.63$ and -0.56 for SPCs and

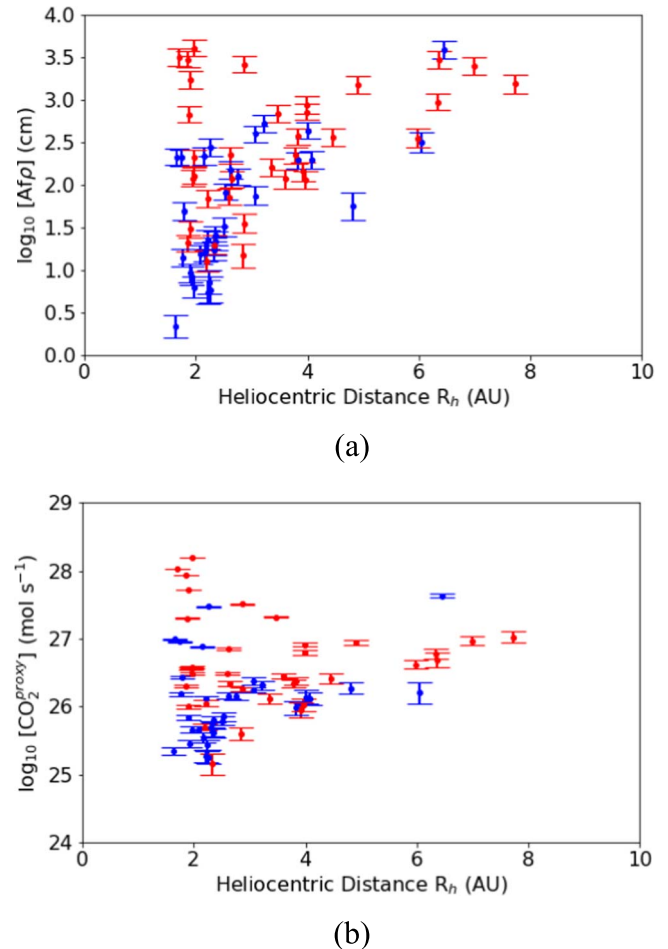


Figure 5. (a) $\log(Af\rho)$ and (b) $\log(Q_{\text{CO}_2}^{\text{proxy}})$ as a function of the heliocentric distance for SPCs (blue) and LPCs (red).

LPCs, respectively. The results of the Spearman test were $\rho_s = -0.81$ and -0.76 for SPCs and LPCs, respectively. The results indicated a potential anticorrelation between $Q_{\text{CO}_2}^{\text{proxy}}/Af\rho$ and R_h . The results are in agreement with Bauer et al. (2015).

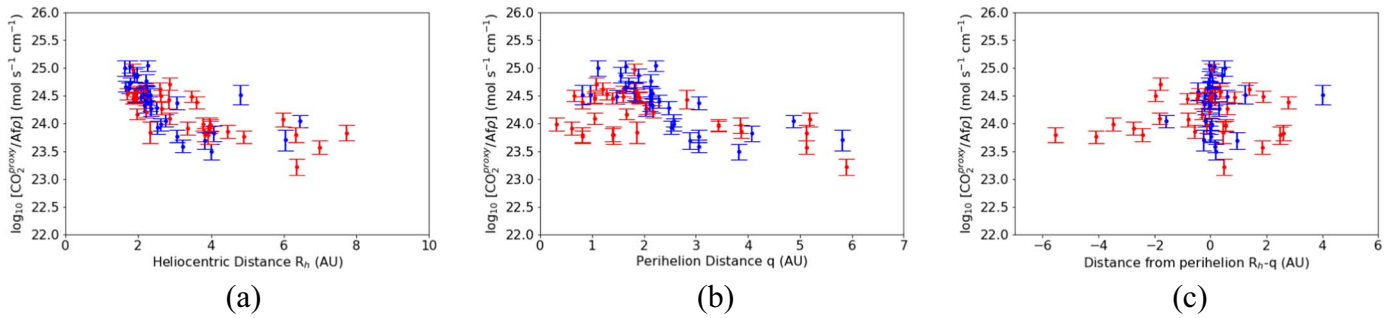


Figure 6. The $\log(Q_{\text{CO}_2}^{\text{proxy}}/Af\rho)$ for SPCs (blue) and LPCs (red) as a function of (a) the heliocentric distance (R_h), (b) perihelion distance (q), and (c) distance from perihelion ($R_h - q$).

For both LPCs and SPCs, the gas-to-dust rate seems to decrease as a function of the heliocentric distance. We find a relation of R_h^{-2} for comets with $R_h < 4$ au. An R_h^{-2} relation is not inconsistent with the proportional amount of energy absorbed by a theoretically exposed fraction of the surface as a function of the comet’s distance from the Sun. The selection bias of the comets discussed in Section 3 limits the sample of this effect inward of ~ 1.7 au, however.

In order to explore the possible source regions or correlations between the gas species, we used the model by Cowan & A’Hearn (1979) to examine whether the CO_2 and H_2O (hereafter also referred to as water in the modeling discussion) were linked and whether it was possible to constrain the source regions of the CO_2 . Several assumptions were made to employ the model, available online from the NASA Planetary Data System’s Small Bodies Node website.⁶ First, our analysis assumes a fixed relative mass ratio of dust mass to gas ejection mass. Second, we presume that three species, CO , CO_2 , and water, are the primary drivers of activity. Third, we examine three kinds of sublimation regions, all with the same albedo ($\sim 5\%$) and emissivity ($\sim 100\%$) characteristics, namely, source regions on a rapidly rotating body, a slowly rotating body near the subsolar point, and an isothermal surface as may be encountered on an icy grain. We tested the case for surface sublimation with equal contributing active areas on the surface for all of the species, or the simple “surface sublimation” model, and found that the water-linked CO_2 production rates were a better match. The actual CO_2 -to-water production rate ratio is less important, since it is the CO_2 that is detected, but the water’s behavior with respect to R_h is the constraining factor, and likewise with the actual dust-to-gas ratios (dimensionless units). We found that the observed drop in $Q_{\text{CO}_2}^{\text{proxy}}/Af\rho$ (Figure 6(a)) is best matched, in terms of steepness and heliocentric distance, by the isothermal surface (grain-like). Furthermore, the CO_2 is likely linked with water emission, and that the sources may better match the grains is in agreement with Harrington Pinto et al. (2022).

The relationship between the perihelion distance q and the gas-to-dust rate $Q_{\text{CO}_2}^{\text{proxy}}/Af\rho$ is shown in Figure 6(b). The results of the Kendall τ test were $\tau = -0.58$ and -0.20 for SPCs and LPCs, respectively. The results of the Spearman test were $\rho_s = -0.77$ and -0.25 for SPCs and LPCs, respectively. The results indicated a potential anticorrelation between $Q_{\text{CO}_2}^{\text{proxy}}/Af\rho$ and q . The SPCs are showing a negative trend between $Q_{\text{CO}_2}^{\text{proxy}}/Af\rho$ and q , while the LPCs are showing a wide and scattered range of values with no trend. The CO or CO_2 volatiles may be more depleted on the

surface of SPCs; therefore, the negative trend may be due to the thermal wave propagating to greater depths at lower perihelion distances accessing a deeper volatile reservoir.

The relationship between the perihelion distance $R_h - q$ and the gas-to-dust rate $Q_{\text{CO}_2}^{\text{proxy}}/Af\rho$ is shown in Figure 6(c). Negative values of $R_h - q$ correspond to when the comet is inbound relative to its perihelion, and positive values are outbound. The results of the Kendall τ test were $\tau = 0.03$ and 0.08 for SPCs and LPCs, respectively. The results of the Spearman test were $\rho_s = 0.05$ and 0.07 for SPCs and LPCs, respectively. The results indicated no correlation between $Q_{\text{CO}_2}^{\text{proxy}}/Af\rho$ and $R_h - q$. However, it seems that at the distance from perihelion near zero, we observe more active SPCs with a wide range of values for the gas-to-dust ratio. Subsurface volatile reservoirs are activated as the thermal wave penetrates to lower depths owing to the comet’s increased insolation at perihelion. The activity observed preperihelion ($R_h - q < 2$ au) and at heliocentric distances $R_h > 4$ au is mainly from LPCs. Hence, while the SPCs may become more depleted in CO or CO_2 over time, the depletion may be less for reservoirs at larger surface depths. The LPCs, in contrast, with considerably fewer perihelion passages, could be relatively pristine, with richer volatile abundances and reservoirs, including for CO , at shallower depths.

5. Summary

We analyze the dust production rate, gas production rate, and gas-to-dust ratio for 57 comets observed within year 1 of the reactivated mission. NEOWISE operates at two wavelengths: 3.4 (W1 band) and 4.6 (W2 band) μm . The sample contains 30 SPCs (including one Centaur) and 27 LPCs. We summarize the major findings that are explained in more detail in Section 4. We found a potential anticorrelation between $Q_{\text{CO}_2}^{\text{proxy}}/Af\rho$ and q , particularly for SPCs. On the surface of an SPC, the CO or CO_2 volatiles might be more depleted, while the subsurface volatiles are activated as the thermal waves propagate to greater depths. This is also in agreement with the fact that we found more active SPCs with a wide range of values for the gas-to-dust ratio at the distance from perihelion $R_h - q$ near zero. We found a potential anticorrelation between $Q_{\text{CO}_2}^{\text{proxy}}/Af\rho$ and R_h . This is consistent with Bauer et al. (2015). Water and CO_2 have a tighter correlation with R_h than water and CO for $0.7 \text{ au} < R_h < 4.6 \text{ au}$. This suggests that the production of CO and CO_2 is different (Harrington Pinto et al. 2022). If we assume that at $R_h < 4.0$ au, the production of water and CO_2 are linked, then the CO_2 production rate is much higher than the dust production because there is sufficient insolation to drive water sublimation (Meech & Svoren 2004). However, outside of 4 au, when CO is the dominant volatile, the water (and liberated CO_2) production would quickly decline. Finally, relative to SPCs, we found more active LPCs at heliocentric distance

⁶ <https://pdssbn.astro.umd.edu/tools/ma-evap/index.shtml>

$R_h > 4$ au and at the distance from perihelion $R_h - q < -2$ au. We also found that SPCs tended to become more active at or after perihelion. The LPCs have fewer passages around perihelion and are therefore more pristine, with potentially richer volatile abundances and reservoirs at shallower depths.

This publication makes use of data products from NEO-WISE, which is a project of JPL/Caltech, funded by the Planetary Science Division of NASA.

ORCID iDs

Adeline Gicquel  <https://orcid.org/0000-0002-9347-8753>
 James M. Bauer  <https://orcid.org/0000-0001-9542-0953>
 Emily A. Kramer  <https://orcid.org/0000-0003-0457-2519>
 Amy K. Mainzer  <https://orcid.org/0000-0002-7578-3885>
 Joseph R. Masiero  <https://orcid.org/0000-0003-2638-720X>

References

- Bauer, J. M., Gicquel, A., Kramer, E., & Meech, K. J. 2021, *PSJ*, **2**, 34
 Bauer, J. M., Grav, T., Blauvelt, E., et al. 2013, *ApJ*, **773**, 22
 Bauer, J. M., Grav, T., Fernandez, Y. R., et al. 2017, *AJ*, **154**, 53
 Bauer, J. M., Stevenson, R., Kramer, E., et al. 2015, *ApJ*, **814**, 85
 Bockelée-Morvan, D., Crovisier, J., Mumma, M. J., & Weaver, H. A. 2004, in *Comets II*, ed. M. C. Festou, H. U. Keller, & H. A. Weaver (Tucson, AZ: Univ. Arizona Press), 391
 Boogert, A. C. A., Gerakines, P. A., & Whittet, D. C. B. 2015, *ARA&A*, **53**, 541
 Cowan, J. J., & A'Hearn, M. F. 1979, *M&P*, **21**, 155
 Crovisier, J., & Encrenaz, T. 1983, *A&A*, **126**, 170
 Cutri, R. M., Wright, E. L., Conrow, T., et al. 2012, Explanatory Supplement to the WISE All-Sky Data Release Products
 Dello Russo, N., Vervack, R. J., Weaver, H. A., & Lisse, C. M. 2009, *Icar*, **200**, 271
 Fougere, N., Altwegg, K., Berthelier, J. -J., et al. 2016, *A&A*, **588**, A134
 Harrington Pinto, O., Womack, M., Fernandez, Y. R., & Bauer, J. 2022, *PSJ*, **3**, 247
 Mainzer, A., Bauer, J., Cutri, R. M., et al. 2014, *ApJ*, **792**, 30
 Mainzer, A., Bauer, J., Grav, T., et al. 2011, *ApJ*, **731**, 53
 Masci, F. J., & Fowler, J. W. 2009, in *ASP Conf. Ser. 411, Astronomical Data Analysis Software and Systems XVIII*, ed. D. A. Bohlender, D. Durand, & P. Dowler (San Francisco, CA: ASP), 67
 Meech, K. J., & Svoren, J. 2004, in *Comets II*, ed. M. C. Festou, H. U. Keller, & H. A. Weaver (Tucson, AZ: Univ. Arizona Press), 317
 NEOWISE-R Team 2020, NEOWISE-R L1b Images, IPAC, doi:10.26131/IRSA147
 Ootsubo, T., Kawakita, H., Hamada, S., et al. 2012, *ApJ*, **752**, 15
 Reach, W. T., Kelley, M. S., & Vaubaillon, J. 2013, *Icar*, **226**, 777
 Rosser, J. D., Bauer, J. M., Mainzer, A. K., et al. 2018, *AJ*, **155**, 164
 Willacy, K., Turner, N., Bonev, B., et al. 2022, *ApJ*, **931**, 164
 Wright, E. L., Eisenhardt, P. R. M., Mainzer, A. K., et al. 2010, *AJ*, **140**, 1868